






Cite this: *J. Mater. Chem. A*, 2023, 11, 14833

# Cu<sub>2</sub>SiSe<sub>3</sub> as a promising solar absorber: harnessing cation dissimilarity to avoid killer antisites†‡

Adair Nicolson, <sup>a</sup> Seán R. Kavanagh, <sup>ab</sup> Christopher N. Savory, <sup>a</sup>  
Graeme W. Watson <sup>c</sup> and David O. Scanlon <sup>\*a</sup>

Copper-chalcogenides are promising candidates for thin film photovoltaics due to their ideal electronic structure and potential for defect tolerance. To this end, we have theoretically investigated the optoelectronic properties of Cu<sub>2</sub>SiSe<sub>3</sub>, due to its simple ternary composition, and the favourable difference in charge and size between the cation species, limiting antisite defects and cation disorder. We find it to have an ideal, direct bandgap of 1.52 eV and a maximum efficiency of 30% for a 1.5 μm-thick film at the radiative limit. Using hybrid density functional theory, the formation energies of all intrinsic defects are calculated, revealing the p-type copper vacancy as the dominant defect species, which forms a perturbed host state. Overall, defect concentrations are predicted to be low and have limited impact on non-radiative recombination, as a consequence of the p–d coupling and antibonding character at the valence band maxima. Therefore, we propose that Cu<sub>2</sub>SiSe<sub>3</sub> should be investigated further as a potential defect-tolerant photovoltaic absorber.

Received 24th April 2023  
Accepted 19th June 2023

DOI: 10.1039/d3ta02429f

rs.c.li/materials-a

## 1 Introduction

Net greenhouse gas emissions have continued to rise in the last decade, with the largest growth coming from increased CO<sub>2</sub> emissions from the burning of fossil fuels for energy.<sup>3</sup> Solar photovoltaic absorbers are one of the most promising renewable energy technologies for combatting this crisis. In particular, thin-film chalcogenide absorbers have been fervently investigated, offering the possibility of reduced material and processing costs, improved low-light performance and greater manufacturing flexibility as compared to conventional silicon solar cells.<sup>4–6</sup> CdTe and Cu(In,Ga)Se<sub>2</sub> are the current market-leaders in this area; however, these materials suffer from the use of rare/toxic elements. Lead-halide perovskites, which have been at the forefront of photovoltaic research for the last decade, show remarkable defect tolerance, but also have stability and toxicity concerns.<sup>4,7,8</sup> Emerging chalcogenide absorbers, such as Cu<sub>2</sub>ZnSnS<sub>4</sub> (CZTS), have shown reduced

efficiencies due to killer defects and performance-limiting disorder.<sup>9,10</sup> The complex quaternary structure containing similarly-sized cations increases the number of possible defects, with the dominant killer defect Sn<sub>Zn</sub> stabilized by widespread Cu–Zn disorder.<sup>10–13</sup> As a result, CZTS solar cells may already be reaching the limit of their performance, motivating the search for alternative candidate absorbers through high-throughput screening studies.<sup>13,14</sup> These studies search for materials that are earth-abundant, with favorable optoelectronic properties, but ignore the role of defects and disorder.

A variety of copper chalcogenides with suitable bandgaps for visible light absorption have emerged from these coarse screening studies, including CuSb(S,Se)<sub>2</sub>, Cu<sub>2</sub>(Si,Sn)Se<sub>3</sub> and LiCuS.<sup>14,15</sup> To further reduce the number of candidate materials, we can learn from the failures of CZTS to employ several design principles to guide the search for a defect tolerant, diamond-like photovoltaic absorber, which could be integrated into current device architectures. By selecting cations with larger differences in charge and ionic radii, the prevalence of cation disorder and detrimental antisite defects could be reduced. To this end, we computationally investigated Cu<sub>2</sub>SiSe<sub>3</sub> (Si<sup>IV</sup> (*r* = 0.26 Å) and Cu<sup>I</sup> (*r* = 0.6 Å)), which had also been identified to have an ideal bandgap from screening studies using the semi-local mBJ + U DFT functional.<sup>14</sup>

We calculated the electronic and optical properties of Cu<sub>2</sub>SiSe<sub>3</sub> using both hybrid DFT and Green's function (GW) methods, including the radiative efficiency limits and electronic band alignment. Given that defect-induced carrier recombination is the dominant limiting factor for power-conversion efficiencies in emerging PV absorbers,<sup>4</sup> an understanding of the

<sup>a</sup>Thomas Young Centre and Department of Chemistry, University College London, 20 Gordon Street, London WC1H 0AJ, UK. E-mail: d.scanlon@ucl.ac.uk

<sup>b</sup>Thomas Young Centre and Department of Materials, Imperial College London, Exhibition Road, London SW7 2AZ, UK

<sup>c</sup>School of Chemistry and CRANN, Trinity College Dublin, College Green, Dublin 2, Ireland

† Electronic supplementary information (ESI) available: Additional figures describing the electronic structure, defect formation energies, energy lowering distortions, and discussion on the chemical potential space. See DOI: <https://doi.org/10.1039/d3ta02429f>

‡ Calculation data is provided in an online repository at <https://doi.org/10.5281/zenodo.7611652>



intrinsic defect thermodynamics is crucial for establishing an accurate outlook on the potential PV performance. Defect calculations were therefore performed using hybrid DFT to gain a complete picture of the intrinsic defect chemistry. In doing so, we predict  $\text{Cu}_2\text{SiSe}_3$  to contain low concentrations of deleterious defects. We expect our results will inspire further investigations into  $\text{Cu}_2\text{SiSe}_3$  for photovoltaic applications.

## 2 Results

$\text{Cu}_2\text{SiSe}_3$  belongs to the adamantine family of materials,<sup>16</sup> crystallizing into the monoclinic  $Cc$  space group. There are two inequivalent  $\text{Cu}^{\text{I}}$  sites and one  $\text{Si}^{\text{IV}}$  site, each connected to four  $\text{Se}^{\text{II}}$  anions to form corner-sharing tetrahedra, Fig. 1a. The lattice parameters of the conventional unit cell, determined using the HSE06 functional,<sup>17,18</sup> are  $a = 6.70 \text{ \AA}$  (0.4%),  $b = 11.84 \text{ \AA}$  (0.3%),  $c = 6.67 \text{ \AA}$  (0.6%), with percentage errors given with respect to experimental values.<sup>19</sup> Lattice parameters calculated using other DFT functionals are provided in the ESI Section 1.†

Due to the presence of  $\text{Cu}(d)$  states in this system, which are poorly modelled by semi-local DFT,<sup>20</sup> hybrid DFT or the GW approximation must be used to accurately calculate the optoelectronic properties. Moreover, the mBJ + U functional has been shown to underestimate the bandgap of Cu-multinary chalcogenides, with a root-mean-square error of 0.24 eV.<sup>21</sup> Using hybrid DFT (HSE06),  $\text{Cu}_2\text{SiSe}_3$  is calculated to have a direct bandgap of 1.52 eV at the  $\Gamma$  point, with spin orbit coupling reducing the bandgap to 1.49 eV ( $\Delta E_g = 0.03 \text{ eV}$ ). The HSE06 band gap is validated by calculation of the electronic structure using the QSGW method, which includes additional screening effects from electron–hole interactions. The QSGW band gap is 1.580 eV, in excellent agreement with HSE06. Solving the dielectric spectrum of  $\text{Cu}_2\text{SiSe}_3$  within the Random Phase approximation (RPA) and Bethe–Salpeter equation (BSE) using the QSGW self-energy directly separates the renormalization of the band structure due to electron–hole screening from direct excitonic effects, Fig. S2.† Only one sub-gap exciton is found, at 1.42 eV, giving an exciton binding energy of 0.16 eV. Plotting the contributions of individual bands to the 1.42 eV exciton onto the band structure of  $\text{Cu}_2\text{SiSe}_3$ , Fig. S3,† it is evident that the exciton has predominantly Wannier–Mott

character,<sup>22</sup> with dominant contributions arising from the valence and conduction bands around  $\Gamma$ .

As part of the process in manufacturing  $\text{Cu}_2\text{ZnSiSe}_4$ , films of  $\text{Cu}_2\text{SiSe}_3$  were synthesized and a bandgap of 1.4 eV determined using transmission measurements in 2015.<sup>23</sup> These measurements give an indication of the  $\text{Cu}_2\text{SiSe}_3$  bandgap, however the sample contained significant amounts of secondary phases and the synthesis process was not refined for high-quality films.

The orbital-decomposed electronic density of states in Fig. 1b shows that the valence band is made up of Cu  $d$  and Se  $p$  states, with the conduction band predominantly Se  $p$  and Si  $s$ .  $\text{Cu}_2\text{SiSe}_3$  has an antibonding valence band maximum (VBM), illustrated by the Crystal Orbital Hamiltonian Population analysis shown in Fig. S4.† This is typical of materials with occupied (semi-)valence cation orbitals (e.g.  $d^{10} \text{Cu}^{1+}$ ), and is associated with the formation of shallow acceptor defects.<sup>24–27</sup>

The highly dispersive conduction band results in low electron effective masses ( $<0.20 m_0$ ) indicating highly mobile carriers, beneficial for the extraction of minority charge carriers in a p-type absorber. The hole masses have much greater anisotropy, with an effective mass of 1.87  $m_0$  from  $\Gamma$  to  $V$ , but 0.18  $m_0$   $\Gamma$  to  $A$  – revealing fast transport for both carriers in  $\text{Cu}_2\text{SiSe}_3$ . A full breakdown of the calculated effective masses is given in Table 1.

Two metrics for predicting the maximum photovoltaic efficiency were calculated; the spectroscopic limited maximum efficiency and the method of Blank *et al.*, which take into account the bandgap and the absorption coefficient of a material.<sup>28,29</sup> Using these metrics,  $\text{Cu}_2\text{SiSe}_3$  reaches a maximum efficiency of 30% at a thickness of 1.5  $\mu\text{m}$ , with a Lambertian structured surface (to reduce scattering) increasing efficiency at thinner film thicknesses (Fig. 2a).

Table 1 Calculated carrier effective masses for  $\text{Cu}_2\text{SiSe}_3$  using HSE06 hybrid DFT

Hole ( $m_0$ )			Electron ( $m_0$ )		
$\Gamma \rightarrow Y$	$\Gamma \rightarrow V$	$\Gamma \rightarrow A$	$\Gamma \rightarrow Y$	$\Gamma \rightarrow V$	$\Gamma \rightarrow A$
0.92	1.87	0.18	0.20	0.19	0.14

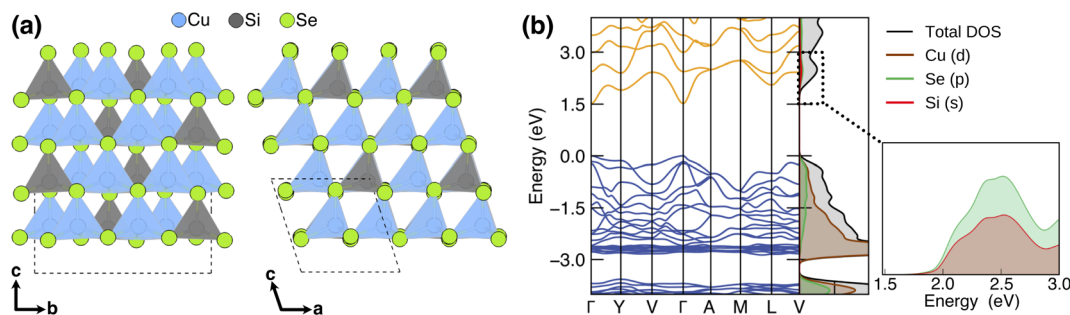


Fig. 1 (a) Crystal structure of  $\text{Cu}_2\text{SiSe}_3$ , with a single conventional unit cell marked by the dashed line; the atoms are colored as follows: Cu = blue, Si = gray, Se = green. Structure visualized in VESTA.<sup>1</sup> (b) Electronic band structure alongside the total and orbital-decomposed density of states calculated using HSE06 ( $E_g = 1.52 \text{ eV}$ ). Valence band marked in blue, conduction band in orange, valence band maximum (VBM) set to 0 eV. The total density of states is not shown in the inset, to aid distinguishing between orbital contributions. Plots generated using SUMO.<sup>2</sup>



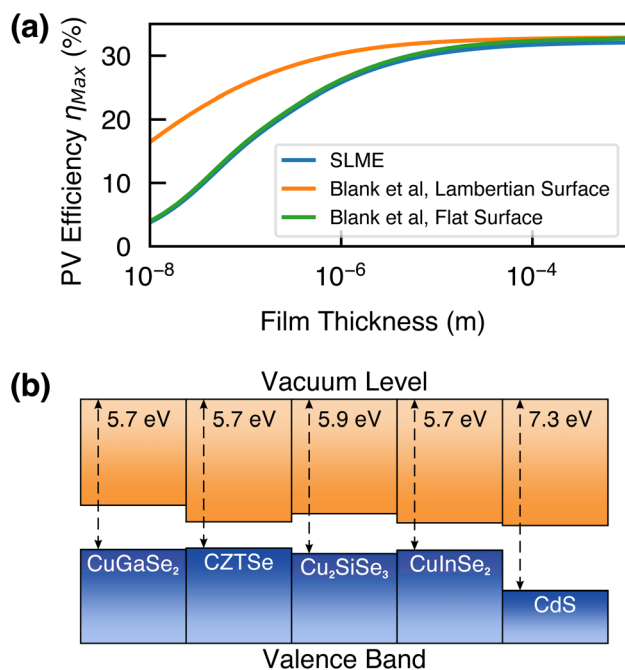


Fig. 2 (a) Maximum PV efficiency ( $\eta_{max}$ ) at the radiative limit as a function of film thickness, calculated using the SLME and Blank *et al.* metrics.<sup>28,29</sup> (b) Electronic band alignment of  $\text{Cu}_2\text{SiSe}_3$  with various Cu-based photovoltaic absorbers and CdS, a commonly used buffer layer. Values (excluding  $\text{Cu}_2\text{SiSe}_3$ ) taken from various experimental and computational ref. 30 and 31.

The calculated band alignment for  $\text{Cu}_2\text{SiSe}_3$  is shown in Fig. 2b. The ionization potential is calculated to be 5.9 eV, similar to other Cu-based absorbers. Thus we can expect  $\text{Cu}_2\text{SiSe}_3$  to be a p-type material and that initial devices could leverage previously-developed device architectures (*e.g.* for CZTSe and CIGSe) for easy fabrication. Due to the high predicted efficiency and composition of non-toxic/earth-abundant

elements,  $\text{Cu}_2\text{SiSe}_3$  is a promising candidate as a photovoltaic absorber, warranting further investigation.

## 2.1 Defect chemistry

To further assess the potential of  $\text{Cu}_2\text{SiSe}_3$  for solar cell operation, an understanding of its defect chemistry is required. High concentrations of deep defects limit the performance of most emerging photovoltaic absorbers. These deep states enable the non-radiative recombination of charge carriers, reducing device efficiencies.<sup>10,32–35</sup> Formation energies for all intrinsic defects of  $\text{Cu}_2\text{SiSe}_3$  were calculated and the transition level diagrams under the most Cu-poor and Cu-rich conditions are shown in Fig. 3. The chemical potential space for  $\text{Cu}_2\text{SiSe}_3$  is bound by seven intersections, with the most Cu-poor regions also being Si-poor, and the most Cu-rich being relatively Si-rich. Formation energy diagrams for the remaining chemical potential limits and a plot of the chemical potential space are provided in the ESI Section 3 and 4.<sup>†</sup>

Most Cu-based absorbers are synthesized under Cu-poor conditions, with  $V_{\text{Cu}}$  being the dominant defect species – although in the case of kesterites (*e.g.* CZTS),  $\text{Cu}_{\text{Zn}}$  antisite defects dominate.<sup>9,36,37</sup> Indeed for  $\text{Cu}_2\text{SiSe}_3$ , we find  $V_{\text{Cu}}$  to have the lowest formation energy and find it to be a shallow acceptor state resulting in  $\text{Cu}_2\text{SiSe}_3$  being intrinsically p-type, with the hole carrier concentrations being of the same order of magnitude as the  $V_{\text{Cu}}$  concentration (Table 2). Annealing to the experimental temperature of 775 K and then quenching to 300 K, the high concentration of  $V_{\text{Cu}}$  places the Fermi level at  $-0.03$  eV (Cu-poor) and  $0.07$  eV (Cu-rich) relative to the VBM (Fig. 4). Through careful control of the annealing temperature and cooling rate the position of the Fermi level and hence the carrier concentrations could be tuned.

The DFT supercell approach for calculating defects fails to properly model the bound states of resonant/shallow defects, as their large, delocalized wave functions extend far beyond the

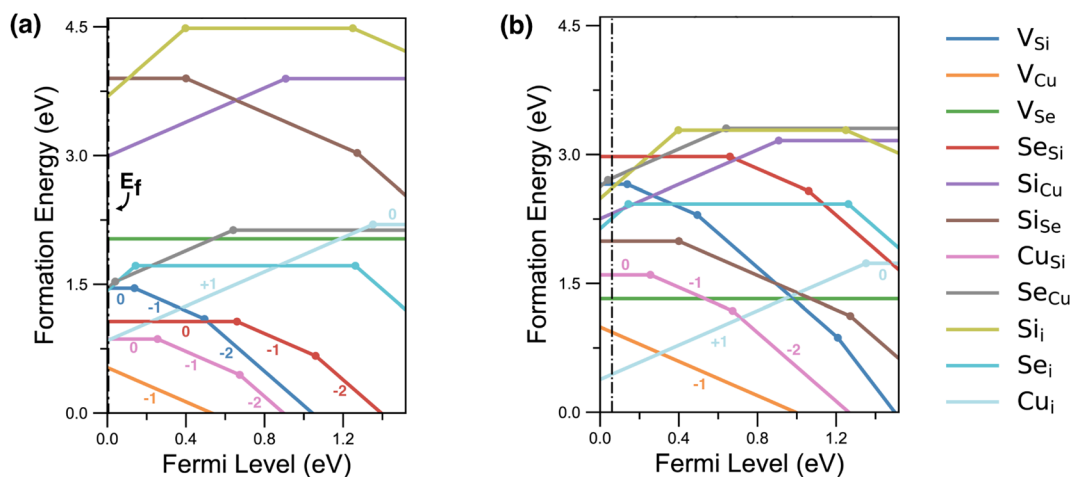


Fig. 3 Formation energies as a function of Fermi level for the intrinsic defects in  $\text{Cu}_2\text{SiSe}_3$  under the most (a) Cu-poor (G) and (b) Cu-rich (D) conditions. G and D correspond to the position on the chemical phase diagram, see ESI Section 3.<sup>†</sup> For each defect species, only the lowest energy defect site has been plotted. Charge state labels only included for defects with low formation energies for clarity. The self-consistent Fermi level is plotted by the dashed black line.



**Table 2** Defect and hole concentrations under Cu-poor and Cu-rich conditions with an annealing temperature of 775 K

Defect species	Concentration (cm <sup>-3</sup> )	
	Cu-poor	Cu-rich
$p_0$	$3 \times 10^{19}$	$8 \times 10^{17}$
$V_{Cu}$	$3 \times 10^{19}$	$1 \times 10^{18}$
$V_{Si}$	$7 \times 10^{12}$	$3 \times 10^6$
$V_{Se}$	$5 \times 10^8$	$2 \times 10^{13}$
$Cu_i$	$9 \times 10^{15}$	$3 \times 10^{17}$
$Si_i$	$9 \times 10^{-4}$	$3 \times 10^1$
$Se_i$	$3 \times 10^{11}$	$3 \times 10^6$
$Cu_{Si}$	$4 \times 10^{16}$	$2 \times 10^{12}$
$Se_{Cu}$	$4 \times 10^{11}$	$2 \times 10^2$
$Se_{Si}$	$9 \times 10^{14}$	$3 \times 10^2$
$Si_{Se}$	$7 \times 10^{-4}$	$2 \times 10^9$
$Si_{Cu}$	$5 \times 10^1$	$8 \times 10^4$

supercell length.<sup>38–41</sup> Thus constraining these states to the supercell results in strong finite-size effects and spurious exciton-like interactions. However, several indicators can be used to determine that the defect is a true shallow state. For instance, we find the charge density of the  $V_{Cu}^0$  hole state to be delocalized across the supercell (ESI Section 5†), that the calculated (0/−1) transition level shifts toward the VBM with increasing supercell size, and lastly, that the atomic sites surrounding the vacancy differ in position by less than 0.01 Å between  $V_{Cu}^{-1}$  and  $V_{Cu}^0$ . Indeed, using the screening methods developed by Kumagai *et al.*,<sup>42</sup> we find the  $V_{Cu}^0$  hole state to have similar orbital character to the bulk VBM, demonstrating its hydrogenic perturbed host state (PHS) nature. Therefore, despite the large predicted concentrations for copper vacancies (Table 2), their shallow nature means they will not play a role in non-radiative capture processes.<sup>32</sup>

The lowest formation energy n-type defect is  $Cu_i$ . There are four distinct interstitial sites, with the lowest energy site having the deepest (+/0) donor level, 0.17 eV below the CBM. As a result,  $Cu_i$  may trap charge carriers, however the impact on device

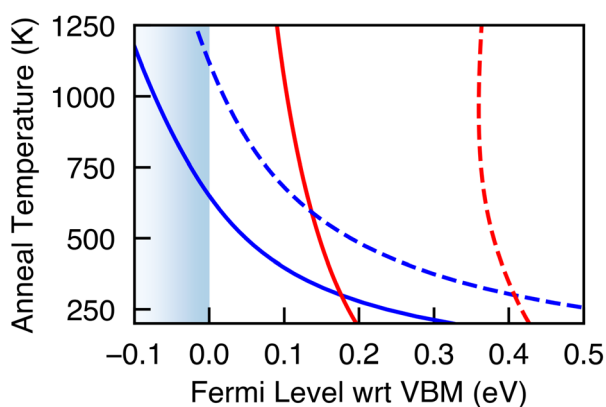


**Fig. 4** Position of the Fermi level during annealing (red) and quenching (blue) under Cu-poor (solid line) and Cu-rich (dashed line) synthesis conditions.

performance is expected to be limited due to slow hole capture.<sup>43,44</sup>

$V_{Se}$  is an ultra-deep donor, with transition levels lying below the VBM – aided by the high energy of the VBM due to Cu d–Se p repulsion, as observed in  $Cu_2ZnSnSe_4$  (CZTSe).<sup>45</sup> While this defect forms in relatively high concentrations under Cu-rich conditions, due to being electronically inactive it should not contribute to non-radiative recombination. The  $Se_{Si}$  antisite defect also has ultra-deep donor states in the valence band, however the defect is additionally found to be stable in the −1 and −2 charge states deep in the band gap. Notably, symmetry-breaking was required to identify the ground-state structures of both  $V_{Se}$  and  $Se_{Si}$  (Fig. S11 and S13†). To stabilize the negative charge states of  $Se_{Si}$  the defect undergoes a significant structural relaxation. The  $Se_{Si}$  defect moves away from the tetrahedrally bonded cation site and forms a trimer with two of the neighboring Se, similar to the reconstructions observed in  $Sb_2Se_3$ .<sup>46</sup> As a result, this defect site could act as a non-radiative recombination center, however to quantitatively determine its impact, this would require the calculation of its carrier capture cross-section.<sup>32</sup>

The remaining defect states with a formation energy below 1.5 eV, which will form in significant concentrations depending on the growth conditions, are the  $Cu_{Si}$  antisite and  $V_{Si}$ . These defects behave similarly due to the ShakeNBreak<sup>47,48</sup> method finding that the lowest energy configuration of a  $V_{Si}$  defect is actually a  $Cu_{Si} + V_{Cu}$  complex. This rearrangement occurs due to the high  $Si^{IV}$  oxidation state, resulting in it being unfavorable to leave the site unoccupied and the low energy of formation of a  $V_{Cu}$  leading to a mobile cation. Thus, both  $Cu_{Si}$  and  $V_{Si}$  defects have similar deep-lying levels. However, the carrier capture cross-sections are expected to be very small due to weak structural relaxation between defect charge states, with the bonds surrounding the defect site distorting by less than 0.02 Å upon charge capture/emission. The lack of distortion between charge states can be explained by considering the orbital make-up of the valence band and  $Cu_{Si}$ . As Cu and Si are tetrahedrally-coordinated by Se, this gives rise to the same Cu d–Se p anti-bonding interaction as found at the VBM. Thus in the fully-ionised charge state ( $Cu_{Si}^{-3}$ ), the occupied anti-bonding defect levels lie above the VBM due to Coulomb repulsion, resulting in deep transition levels. Consequently, it is favorable to remove electrons and depopulate the anti-bonding levels, placing holes in the Cu d–Se p states (ESI Fig. S10†). The reduction in charge lowers the energy of the defect states, resulting in them being more VBM-like and making  $q = 0, -1$  and  $-2$  the stable charge states for  $Cu_{Si}$ .

Overall, our results find the formation energy of antisite defects to be significantly larger than in CIGS and kesterite materials (*e.g.*  $Cu_{Zn}$  defects has a formation energy of 0.4 eV in CZTS), due to larger valence and size differences between the cation species (*i.e.*  $Si^{IV}$  ( $r = 0.26$  Å) and  $Cu^I$  ( $r = 0.6$  Å) vs.  $Sn^{IV}$  ( $r = 0.55$  Å) and  $Zn^{II}$  ( $r = 0.6$  Å) in CZTS, where  $Sn_{Zn}$  are the killer defects).<sup>36,49,50</sup> This would have the added benefit of reducing cation disorder in  $Cu_2SiSe_3$  which has been shown to lower the formation energy of defects in CZTS.<sup>13</sup> All remaining defect species not discussed in detail have too high formation energies





to form in sufficient concentrations to significantly affect device performance. Our study of the intrinsic defect in  $\text{Cu}_2\text{SiSe}_3$  shows that the antibonding VBM, often associated with defect-tolerance, indeed contributes to the formation of electrically benign defects,<sup>51</sup> borne out by the  $V_{\text{Cu}}$  and  $V_{\text{Se}}$  discussed earlier. This paints a promising picture for potential defect tolerance in this compound.

### 3 Conclusion

In this work, we have investigated  $\text{Cu}_2\text{SiSe}_3$  as a candidate photovoltaic absorber, determining its bandgap to be 1.52 eV using HSE06. A maximum efficiency of 30% at the radiative limit is predicted for thin film devices, and we expect current copper-chalcogenide device architectures to be readily transferable. Using hybrid density functional theory, all intrinsic defect sites were investigated, with the lowest energy defects ( $V_{\text{Cu}}$  and  $\text{Cu}_i$ ) expected to be benign with respect to carrier recombination. As a result,  $\text{Cu}_2\text{SiSe}_3$  shows great promise as a potential defect-tolerant photovoltaic absorber, however further calculations of capture cross-sections are required. We believe this work serves as a promising outlook on the potential solar cell application of this material, and hope that it encourages experimentalists working in the field of emerging photovoltaics to synthesize and investigate  $\text{Cu}_2\text{SiSe}_3$  devices.

### 4 Methods

All calculations were performed using periodic DFT within the Vienna *Ab Initio* Simulation Package (VASP).<sup>52–54</sup> This work uses the HSE06 hybrid DFT functional which combines 75% exchange and 100% of the correlation energy from the Perdew, Burke, and Ernzerhof (PBE) semi-local functional with 25% exact Hartree–Fock (HF) exchange at short ranges.<sup>17,18,55</sup> HSE06 has been shown to accurately reproduce the electronic structure and properties of many small bandgap semiconductors, including Cu-multinary chalcogenide semiconductors.<sup>21</sup> A plane wave energy cutoff of 350 eV was used and  $k$ -points were sampled with a  $\Gamma$  centered  $4 \times 4 \times 4$  mesh for the 12-atom primitive cell. The total energy was converged to less than 1 meV per atom with these parameters, and a force tolerance of 0.01 eV  $\text{\AA}^{-1}$  was used during geometry relaxation. The plane wave cutoff was increased to 500 eV during structural relaxation to avoid errors arising from Pulay stress. A denser  $6 \times 6 \times 6$   $k$ -point mesh was used for the calculation of the optical properties, and a larger number of unoccupied bands were included in the calculation (NBANDS increased to 100). Upper limits to the photovoltaic efficiency were determined from the HSE06 electronic and optical calculations, using both the ‘Spectroscopic Limited Maximum Efficiency’ (SLME) metric and the method of Blank *et al.*<sup>28,29</sup> To calculate the electronic band alignment, the core level alignment method was used with surfaces generated by surface.<sup>56,57</sup>

Defect calculations were performed in a 96-atom supercell created by the expansion of the primitive unit cell with the matrix:

$$\begin{pmatrix} 2 & -2 & 0 \\ 1 & 1 & 0 \\ 1 & -1 & 2 \end{pmatrix}$$

and was sampled with a  $\Gamma$ -centered  $2 \times 2 \times 2$   $k$ -point mesh. The lattice parameters of this supercell were  $a = 13.41 \text{ \AA}$ ,  $b = 11.84 \text{ \AA}$ ,  $c = 12.97 \text{ \AA}$  and angles  $\alpha = 90.0^\circ$ ,  $\beta = 78.4^\circ$ ,  $\gamma = 90.0^\circ$ . All inequivalent vacancy and antisite defect sites were considered, and Voronoi tessellation was used to determine potential interstitial sites.<sup>58</sup> Overall, this came to six vacancies, nine antisites and 51 interstitials (Table S3†). To aid the search for the ground state structures, the ShakeNBreak package was used to implement the bond distortion methodology to find any energy-lowering reconstructions at defect sites.<sup>47,48</sup> This structure-searching method uses nearest-neighbour bond distortions, along with random atomic perturbations, in order to find the lowest energy structure. Each defect was distorted up to a bond distortion factor of  $\pm 0.4$ , in increments of 0.1. In order to account for spurious interactions between charged defects and their periodic image in the DFT supercell approach, the eFNV charge correction scheme was employed.<sup>59,60</sup> Formation energies are then calculated for each defect  $X$  in charge state  $q$  using,<sup>61</sup>

$$E^f(X^q) = E_{\text{tot}}(X^q) - E_{\text{tot}}(\text{host}) - \sum_i n_i \mu_i + qE_{\text{F}} = E_{\text{corr}}. \quad (1)$$

where  $E_{\text{tot}}(X^q)$  and  $E_{\text{tot}}(\text{host})$  are the total energies of the defect supercell and pristine supercell.  $\mu_i$  is the chemical potential of species  $i$  and  $n$  is the number of atoms of species  $i$  removed or added to form the defect.  $E_{\text{F}}$  is the Fermi level and finally  $E_{\text{corr}}$  is the charge correction term.

Defect concentrations were determined through the calculation of the self-consistent Fermi level as implemented in *py-sc-fermi*.<sup>62,63</sup> Typically materials are grown/annealed at elevated temperatures (as is the case for  $\text{Cu}_2\text{SiSe}_3$  (ref. 19, 23 and 64)), where defects form, before cooling to room temperature. Thus, to simulate annealing and quenching, the equilibrium defect concentrations are calculated self-consistently at various annealing temperatures. Next, to simulate quenching the sample to room temperature, the calculated defect concentrations are held constant, while the charge states and Fermi level are allowed to re-equilibrate at 300 K. A schematic outlining the workflow is included in the ESI (Fig. S7†).

Many-body perturbation theory calculations were performed within the Questaal package,<sup>65</sup> using the QSGW method of Kotani *et al.*<sup>66</sup> together with the modification to include ladder diagrams within the screened Coulomb interaction  $W$ , herein referred to as QSG $\dot{W}$ .<sup>67,68</sup> The HSE06 ground state structure was used throughout. Muffin tin radii of 2.37 a.u., 2.07 a.u., and 2.17 a.u. were used for Cu, Si and Se respectively, with an  $l$ -cutoff of 4 used for all atoms. A  $k$ -mesh of  $4 \times 4 \times 4$  and a  $G$ -cutoff for the interstitial plane waves of 8.0  $\text{Ry}^{\frac{1}{2}}$  was used for the convergence of the QSGW and QSG $\dot{W}$  self-energies, with a finer  $8 \times 8 \times 7$  mesh used for intermediate DFT calculations. The QSG $\dot{W}$  band gap was found to converge to within 0.01 eV using 12 occupied and 12 empty bands, while a finer  $6 \times 6 \times 6$  was used for the



solution of the Bethe–Salpeter Equation and the resultant dielectric spectrum.

## Conflicts of interest

There are no conflicts to declare.

## Acknowledgements

We acknowledge Bodo Batnaran for sharing data which was useful for comparisons in the early stages of this project. A. N. and S. R. K. acknowledge the EPSRC and SFI Centre for Doctoral Training in Advanced Characterisation of Materials (EP/S023259/1) for funding a PhD studentship. C. N. S. is grateful to the Department of Chemistry at UCL and the Ramsay Memorial Fellowship Trust for the funding of a Ramsay Fellowship. The authors acknowledge the use of the UCL Kathleen and Thomas High Performance Computing Facility. Via membership of the UK's HEC Materials Chemistry Consortium, which is funded by the EPSRC (EP/L000202, EP/R029431, EP/T022213), this work used the ARCHER2 UK National Supercomputing Service (<http://www.archer2.ac.uk/>) and the UK Materials and Molecular Modelling (MMM) Hub (Thomas – EP/P020194 & Young – EP/T022213).

## Notes and references

- 1 K. Momma and F. Izumi, *J. Appl. Crystallogr.*, 2008, **41**, 653–658.
- 2 A. M. Ganose, A. J. Jackson and D. O. Scanlon, *J. Open Source Softw.*, 2018, **3**, 717.
- 3 IPCC, *Climate Change 2022: Mitigation of Climate Change. Contribution of Working Group III to the Sixth Assessment Report of the Intergovernmental Panel on Climate Change*, Cambridge University Press, Cambridge, UK and New York, NY, USA, 2022, DOI: [10.1017/9781009157926](https://doi.org/10.1017/9781009157926).
- 4 Y.-T. Huang, S. R. Kavanagh, D. O. Scanlon, A. Walsh and R. L. Z. Hoyer, *Nanotechnology*, 2021, **32**, 132004.
- 5 S. Hadke, M. Huang, C. Chen, Y. F. Tay, S. Chen, J. Tang and L. Wong, *Chem. Rev.*, 2022, **122**(11), 10170–10265.
- 6 K. V. Sopiha, C. Comparotto, J. A. Márquez and J. J. S. Scragg, *Adv. Opt. Mater.*, 2022, **10**, 2101704.
- 7 A. M. Ganose, C. N. Savory and D. O. Scanlon, *Chem. Commun.*, 2016, **53**, 20–44.
- 8 R. Nie, R. R. Sumukam, S. H. Reddy, M. Banavoth and S. I. Seok, *Energy Environ. Sci.*, 2020, **13**, 2363–2385.
- 9 S. Chen, X. G. Gong, A. Walsh and S.-H. Wei, *Appl. Phys. Lett.*, 2010, **96**, 021902.
- 10 S. Kim, J. A. Márquez, T. Unold and A. Walsh, *Energy Environ. Sci.*, 2020, **13**, 1481–1491.
- 11 S. Schorr, G. Gurieva, M. Guc, M. Dimitrievska, A. Pérez-Rodríguez, V. Izquierdo-Roca, C. S. Schnohr, J. Kim, W. Jo and J. M. Merino, *J. Phys.: Energy*, 2019, **2**, 012002.
- 12 L. L. Baranowski, P. Zawadzki, S. Lany, E. S. Toberer and A. Zakutayev, *Semicond. Sci. Technol.*, 2016, **31**, 123004.
- 13 W. Chen, D. Dahliah, G.-M. Rignanese and G. Hautier, *Energy Environ. Sci.*, 2021, **14**, 3567–3578.
- 14 Y. Zhang, Y. Wang, J. Zhang, L. Xi, P. Zhang and W. Zhang, *J. Chem. Phys.*, 2016, **144**, 194706.
- 15 D. Dahliah, G. Brunin, J. George, V.-A. Ha, G.-M. Rignanese and G. Hautier, *Energy Environ. Sci.*, 2021, **14**, 5057–5073.
- 16 B. Pamplin, *Prog. Cryst. Growth Charact.*, 1980, **3**, 179–192.
- 17 J. Heyd, G. E. Scuseria and M. Ernzerhof, *J. Chem. Phys.*, 2003, **118**, 8207–8215.
- 18 A. V. Krukau, O. A. Vydrov, A. F. Izmaylov and G. E. Scuseria, *J. Chem. Phys.*, 2006, **125**, 224106.
- 19 X.-a. Chen, H. Wada, A. Sato and H. Nozaki, *J. Alloys Compd.*, 1999, **290**, 91–96.
- 20 F. Oba and Y. Kumagai, *Appl. Phys. Express*, 2018, **11**, 060101.
- 21 Q. Wang, H. Ma, B. Ni, Y. Li, S. Huang, W. Lin and Y. Zhang, *J. Phys. Chem. C*, 2022, **126**, 4684–4697.
- 22 S. R. Kavanagh, C. N. Savory, S. M. Liga, G. Konstantatos, A. Walsh and D. O. Scanlon, *J. Phys. Chem. Lett.*, 2022, 10965–10975.
- 23 H. ElAnzeery, M. Buffière, K. B. Messaoud, S. Oueslati, G. Brammertz, O. E. Daif, D. Cheyins, R. Guindi, M. Meuris and J. Poortmans, *Phys. Status Solidi – Rapid Res. Lett.*, 2015, **9**, 338–343.
- 24 A. Zakutayev, C. M. Caskey, A. N. Fioretti, D. S. Ginley, J. Vidal, V. Stevanovic, E. Tea and S. Lany, *J. Phys. Chem. Lett.*, 2014, **5**, 1117–1125.
- 25 S. B. Zhang, S.-H. Wei, A. Zunger and H. Katayama-Yoshida, *Phys. Rev. B: Condens. Matter Mater. Phys.*, 1998, **57**, 9642–9656.
- 26 A. Walsh and A. Zunger, *Nat. Mater.*, 2017, **16**, 964–967.
- 27 Y.-T. Huang, S. R. Kavanagh, M. Righetto, M. Rusu, I. Levine, T. Unold, S. J. Zelewski, A. J. Sneyd, K. Zhang, L. Dai, A. J. Britton, J. Ye, J. Julin, M. Napari, Z. Zhang, J. Xiao, M. Laitinen, L. Torrente-Murciano, S. D. Stranks, A. Rao, L. M. Herz, D. O. Scanlon, A. Walsh and R. L. Z. Hoyer, *Nat. Commun.*, 2022, **13**, 4960.
- 28 L. Yu and A. Zunger, *Phys. Rev. Lett.*, 2012, **108**, 068701.
- 29 B. Blank, T. Kirchartz, S. Lany and U. Rau, *Phys. Rev. Appl.*, 2017, **8**, 024032.
- 30 S. Chen, A. Walsh, J.-H. Yang, X. G. Gong, L. Sun, P.-X. Yang, J.-H. Chu and S.-H. Wei, *Phys. Rev. B: Condens. Matter Mater. Phys.*, 2011, **83**, 125201.
- 31 R. K. Swank, *Phys. Rev.*, 1967, **153**, 844–849.
- 32 A. Alkauskas, Q. Yan and C. G. Van de Walle, *Phys. Rev. B: Condens. Matter Mater. Phys.*, 2014, **90**, 075202.
- 33 A. Alkauskas, M. D. McCluskey and C. G. Van de Walle, *J. Appl. Phys.*, 2016, **119**, 181101.
- 34 S. R. Kavanagh, D. O. Scanlon, A. Walsh and C. Freysoldt, *Faraday Discuss.*, 2022, **239**, 339–356.
- 35 S. R. Kavanagh, A. Walsh and D. O. Scanlon, *ACS Energy Lett.*, 2021, **6**, 1392–1398.
- 36 C. Persson, Y.-J. Zhao, S. Lany and A. Zunger, *Phys. Rev. B: Condens. Matter Mater. Phys.*, 2005, **72**, 035211.
- 37 C. Rincón and R. Márquez, *J. Phys. Chem. Solids*, 1999, **60**, 1865–1873.
- 38 S. Lany and A. Zunger, *J. Appl. Phys.*, 2006, **100**, 113725.
- 39 G. Zhang, A. Canning, N. Grønbech-Jensen, S. Derenzo and L.-W. Wang, *Phys. Rev. Lett.*, 2013, **110**, 166404.



- 40 Y. Zhang, A. Mascarenhas and L.-W. Wang, *Phys. Rev. B: Condens. Matter Mater. Phys.*, 2006, **74**, 041201.
- 41 M. W. Swift, H. Peelaers, S. Mu, J. J. L. Morton and C. G. Van de Walle, *npj Comput. Mater.*, 2020, **6**, 1–9.
- 42 Y. Kumagai, N. Tsunoda, A. Takahashi and F. Oba, *Phys. Rev. Mater.*, 2021, **5**, 123803.
- 43 W. Shockley and W. T. Read, *Phys. Rev.*, 1952, **87**, 835–842.
- 44 R. N. Hall, *Phys. Rev.*, 1952, **87**, 387.
- 45 S. Kim, J.-S. Park and A. Walsh, *ACS Energy Lett.*, 2018, **3**, 496–500.
- 46 X. Wang, S. R. Kavanagh, D. O. Scanlon and A. Walsh, *Four-Electron Negative-U Vacancy Defects in Antimony Selenide*, 2023, <http://arxiv.org/abs/2302.04901>.
- 47 I. Mosquera-Lois, S. R. Kavanagh, A. Walsh and D. O. Scanlon, *J. Open Source Softw.*, 2022, **7**, 4817.
- 48 I. Mosquera-Lois, S. R. Kavanagh, A. Walsh and D. O. Scanlon, *npj Comput. Mater.*, 2023, **9**, 1–11.
- 49 R. D. Shannon, *Acta Crystallogr., Sect. A: Cryst. Phys., Diffraction, Theor. Gen. Crystallogr.*, 1976, **32**, 751–767.
- 50 S. Kim, J.-S. Park, S. N. Hood and A. Walsh, *J. Mater. Chem. A*, 2019, **7**, 2686–2693.
- 51 R. E. Brandt, J. R. Poindexter, P. Gorai, R. C. Kurchin, R. L. Z. Hoye, L. Nienhaus, M. W. B. Wilson, J. A. Polizzotti, R. Sereika, R. Žaltauskas, L. C. Lee, J. L. MacManus-Driscoll, M. Bawendi, V. Stevanović and T. Buonassisi, *Chem. Mater.*, 2017, **29**, 4667–4674.
- 52 G. Kresse and J. Hafner, *Phys. Rev. B: Condens. Matter Mater. Phys.*, 1993, **47**, 558–561.
- 53 G. Kresse and J. Furthmüller, *Phys. Rev. B: Condens. Matter Mater. Phys.*, 1996, **54**, 11169–11186.
- 54 G. Kresse and D. Joubert, *Phys. Rev. B: Condens. Matter Mater. Phys.*, 1999, **59**, 1758–1775.
- 55 J. P. Perdew, K. Burke and Y. Wang, *Phys. Rev. B: Condens. Matter Mater. Phys.*, 1996, **54**, 16533–16539.
- 56 S.-H. Wei and A. Zunger, *Appl. Phys. Lett.*, 1998, **72**, 2011–2013.
- 57 K. Brlec, D. W. Davies and D. O. Scanlon, *J. Open Source Softw.*, 2021, **6**, 3171.
- 58 A. Kononov, C.-W. Lee, E. P. Shapera and A. Schleife, *J. Phys.: Condens. Matter*, 2023, **35**, 334002.
- 59 Y. Kumagai and F. Oba, *Phys. Rev. B: Condens. Matter Mater. Phys.*, 2014, **89**, 195205.
- 60 C. Freysoldt, J. Neugebauer and C. G. Van de Walle, *Phys. Rev. Lett.*, 2009, **102**, 016402.
- 61 C. G. Van de Walle and J. Neugebauer, *J. Appl. Phys.*, 2004, **95**, 3851–3879.
- 62 J. Buckeridge, *Comput. Phys. Commun.*, 2019, **244**, 329–342.
- 63 A. G. Squires, D. O. Scanlon and B. J. Morgan, *J. Open Source Softw.*, 2023, **8(82)**, 4962.
- 64 G. Brammertz, B. Vermang, H. ElAnzeery, S. Sahayaraj, S. Ranjbar, M. Meuris and J. Poortmans, *Phys. Status Solidi C*, 2017, **14**, 1600162.
- 65 D. Pashov, S. Acharya, W. R. Lambrecht, J. Jackson, K. D. Belashchenko, A. Chantis, F. Jamet and M. van Schilfgarde, *Comput. Phys. Commun.*, 2020, **249**, 107065.
- 66 T. Kotani, M. van Schilfgarde and S. V. Faleev, *Phys. Rev. B: Condens. Matter Mater. Phys.*, 2007, **76**, 165106.
- 67 B. Cunningham, M. Grüning, P. Azarhoosh, D. Pashov and M. van Schilfgarde, *Phys. Rev. Mater.*, 2018, **2**, 034603.
- 68 B. Cunningham, M. Grüning, D. Pashov and M. van Schilfgarde, QSGW: Quasiparticle Self consistent GW with ladder diagrams in *W*, *arXiv*, 2023, preprint, arXiv:2302.06325v1 [cond-mat.mtrl-sci], DOI: [10.48550/arXiv.2302.06325](https://doi.org/10.48550/arXiv.2302.06325).

